RSC Advances

ROYAL SOCIETY
OF CHEMISTRY

PAPER

View Article Online
View Journal | View Issue

Check for updates

Cite this: *RSC Adv.*, 2021, **11**, 30031

Hierarchical $NaFePO_4$ nanostructures in combination with an optimized carbon-based electrode to achieve advanced aqueous Na-ion supercapacitors†

Sudipta Biswas, [*a] Debabrata Mandal, [b] Trilok Singh [c]
and Amreesh Chandra [abd]

Received 16th July 2021
Accepted 26th August 2021

DOI: 10.1039/d1ra05474k

rsc.li/rsc-advances

Recent trends in sodium-ion-based energy storage devices have shown the potential use of hollow structures as an electrode material to improve the performance of these storage systems. It is shown that, in addition to the use of hierarchical structures, the choice of the complementary carbon electrode determines the final performance of Na-ion-based devices. Here, we present simple synthesis strategies to prepare different structured carbonaceous materials that can be upscaled to an industrial level. Individual carbon materials deliver specific capacitance ranges from 120 to 220 F g^{-1} at a current density of 1 A g^{-1} (with excellent capacity retention). These structures, when combined with hollow $NaFePO_4$ microspheres to fabricate an aqueous supercapacitor, show as high as a 1.7 V working potential window and can deliver a maximum energy density of 25.29 W h kg^{-1} capacity retention. These values are much higher than those reported by $NaFePO_4$ solid particles and randomly chosen carbon structure-based supercapacitors.

Introduction

Na-ions, with chemistry similar to Li-ions, were always expected to deliver characteristics that could be useful for storage technologies.[1] Their limited use today is mostly linked with the difficulties associated with obtaining the single-phase Na-based materials, with high cycling stability.[2,3] Over the last few years, there has been a steady growth in the expertise to stabilize Na-based systems, with simple morphologies and reasonable electrochemical performance.[4] To date, particles with solid morphologies have been normally used in Na-ion supercapacitors. To bring a significant jump in the performance, hierarchical structures will now have to be investigated.[5,6] Additionally, one should be mindful of the fact that Na^+, with a larger ionic radius than Li^+, will not combine with any randomly chosen anode. The complementary electrode must be such that it allows space for efficient ion intercalation and deintercalation. It has also been suggested that to obtain the desired performance from Na-ion storage devices, carbon-based electrodes will have to be carefully tuned.[7]

One of the materials that is being investigated is $NaFePO_4$ (NFP). The hope is that, NFP can deliver performance parameters like $LiFePO_4$ (a famous material in Li-ion battery) and make Na-ion technology competitive with the other similar yet established systems. The formation of single-phase $NaFePO_4$ and its use in Na-ion batteries have been reported over the last few years.[8–11] Being a battery-type material, $NaFePO_4$ has not been investigated much for supercapacitor application. The high-rate capability and structural stability of the olivine phosphates makes these structures useful for energy storage devices. There are many studies present in the literature that deal with conductive coating and metal ion doping to improve the performance.[12] In the current work, the strategy of using morphology driven changes Na-ion supercapacitors was employed.

Many recent studies related to metal oxides suggesting the use of hierarchical nanostructures as a basic ingredient in the next generation supercapacitors.[13,14] Therefore, it is now imperative that hierarchical structures are tested in Na-ion supercapacitors and batteries. This paper deals with the use of hierarchical $NaFePO_4$ in Na-ion supercapacitors. Most studies in literature have remained focus on one combination of Na-based electrodes with a particular carbon-based electrode. Here, it is established that unless a proper combination with

---

[a] *Department of Physics, Indian Institute of Technology Kharagpur, Kharagpur-721302, India. E-mail: sudiptabiswas@gmail.com; sbiswas@iitkgp.ac.in*

[b] *School of Nano Science and Technology, Indian Institute of Technology Kharagpur, Kharagpur-721302, India*

[c] *Functional Materials and Device Laboratory, School of Energy Science & Engineering, Indian Institute of Technology Kharagpur, Kharagpur-721302, India*

[d] *School of Energy Science & Engineering, Indian Institute of Technology Kharagpur, Kharagpur-721302, India*

† Electronic supplementary information (ESI) available. See DOI: 10.1039/d1ra05474k

a suitable carbon structure-based electrode is determined, the device does not deliver the required characterization. Using a combination of NFP with activated carbon (AC), carbon microsphere (CMS), carbon nanosphere (CNS), graphene oxide (GO), reduced graphene oxide (rGO), graphene quantum dots, and nitrogen-doped graphene quantum dots, it is shown that NFP//rGO is the best option. Reasons are given to explain the properties of rGO, which helps it to supersede others. The studies clearly show that Na-ion supercapacitors can only become useful if the carbon-based negative electrode is carefully chosen. Further, for different Na-ion-based electrode materials, the desired carbon structures would be different.

Experimental

Material synthesis

AC was purchased from Merck Industries Pvt. Ltd. and used without any further modifications. CMS and CNS were synthesized by the hydrothermal method by controlling the precursor concentration and reaction time. For GO, a modified Hummer's method was used. Then these GOs were reduced with the help of the $NaBH_4$ to obtain rGO. GQD was prepared by the pyrolysis technique utilizing citric acid and later it was nitrogen-doped by ammonia solution. Hollow $NaFePO_4$ was synthesized by a one-pot hydrothermal facile route.[15] Detailed synthesis procedures for obtaining materials used in this study are discussed in the ESI.†[16,17]

Electrode preparation and characterization

Slurries were prepared using active material, polyvinylidene fluoride-*co*-hexafluoropropylene (PVDF) binder in acetone (for carbon structures), and *N*-methyl-2-pyrrolidone (for $NaFePO_4$) as a mixing media. The ratio was 8 : 1 : 1 for active material, PVDF, and AC, respectively. The obtained slurries were drop casted onto the graphite sheets (with 1 cm × 1 cm) and vacuum dried at 80 °C for 12 h. All electrochemical measurements were performed using 2 M aqueous NaOH as an electrolyte.[18] Current collecting graphite sheet coated with slurries containing the active materials was used. Platinum wire and Ag/AgCl (in 3.0 M KCl) were used as the counter and reference electrodes, respectively. CR2032 type asymmetric cells were fabricated using a Whatman glass fiber as the separator and the respective electrodes on either side. 3-electrode measurements were performed to optimize the electrochemical window of each electrode. The best performing electrolyte was also selected by the performance obtained from the 3-electrode measurements. After optimizing the electrodes, NFP and carbon electrodes were used the positive and negative electrodes, respectively, in a device.

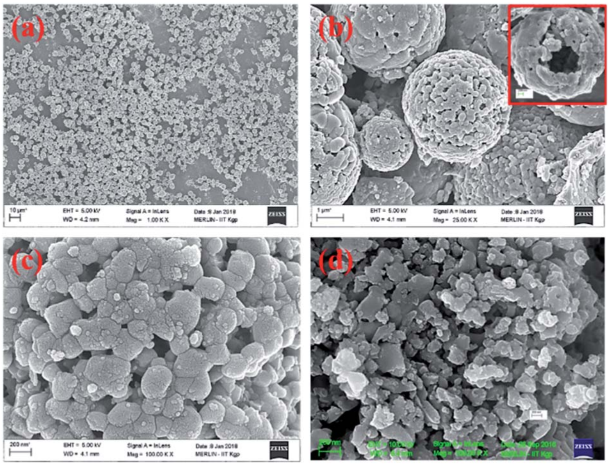

Fig. 1 SEM micrographs of (a–c) hollow and (d) solid $NaFePO_4$.

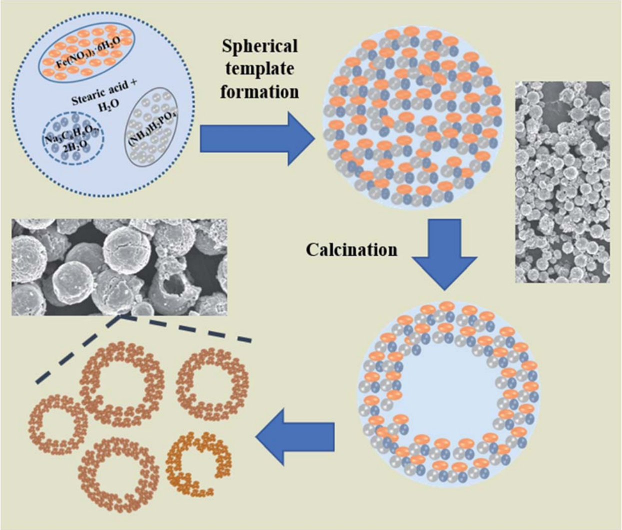

Scheme 1 Growth mechanism of hollow $NaFePO_4$.

Result and discussion

Physiochemical results

The X-ray diffraction pattern of $NaFePO_4$ (NFP) could be indexed using the JCPDS card no. 04-012-9665, representing an orthorhombic unit cell with *Pnmb* space group as shown in Fig. S1(a).† Fig. 1(a–c) shows the SEM images of NFP, where a distinct hollow cavity is visible. The size of the synthesized NFP microspheres varied in the range of 1–3 μm. Corresponding TEM micrographs are shown in Fig. S1(b).† Such structures are known to have advantages of higher surface area, large pore size, and transport channels in comparison to their solid counterparts.[19] The growth of these spherical particles is the resultant of reagent reaction and kinetically controlled diffusion (Scheme 1). The details are given in ESI.†

To prove the advantage of hollow hierarchical structure, solid nanostructures were also synthesized using an auto combustion route. A typical solid disc-type morphology of NFP

Table 1 Crystal parameters for $NaFePO_4$

Parameter	*a* (Å)	*b* (Å)	*c* (Å)	Cell volume (Å^3)
Hollow NFP	7.67	8.76	5.12	343.84
Solid NFP	7.62	8.78	5.11	341.89

is shown in Fig. 1(d). The lattice parameters listed in Table 1, clearly showed that the two morphologies had similar dimensions. Therefore, any change in electrochemical performance would primarily originate from the change in the surface area.

BET measurement showed that the surface area of hollow particles was 20.1 $m^2 g^{-1}$, with an average pore size of 6 nm (see Fig. S2†). In comparison, solid structures had a surface area of 6.1 $m^2 g^{-1}$, with an average pore size of 1.58 nm. The particle size was further confirmed by the SEM analysis, which indicated the average particle size was 1.527 μm (see Fig. S3(a)†). FTIR spectra of the sample also supported the presence of the $[PO_4]^{3-}$ group in the material. This would provide stability to the structure (see Fig. S3(c and d)†).[20] The atomic ratio of Na : Fe : P : O was found to be 1.05 : 1 : 1.08 : 3.57 from the EDAX analysis, which confirmed the formation of $NaFePO_4$ (see Fig. S4†). Further, the average zeta potential, obtained from the material dispersed in methanol, was −41 mV (see Fig. S3(b)†). This indicated that the $NaFePO_4$ could be used as a promising positive electrode.

Fig. S5(a)† shows the X-ray diffraction pattern of all the carbon structures used during this work. The peak near 25° is the characteristic (002) plane of graphite.[21] The broadness of the peak qualitatively showed the amorphous nature of the material. Phase purity and crystallinity of GO were also checked by XRD, where it exhibited a sharp peak near 10.52°, corresponding to the (001) basal plane with a *d* spacing of 0.422 nm.[21] This is due to the presence of hydroxyl, epoxy and carbonyl groups are present in the GO structure.

AC has a higher surface area due to surface modification and the availability of smaller pores.[22] Fig. 2(a–c) and inset of Fig. 2(a–c) show the SEM and TEM micrographs of the different carbon structures. Fig. S6(a1, a2, b1 and b2)† show the SEM and TEM of other carbon structures. The micrographs showed that the flake-type structures remained the same, even after reduction. AFM images of the graphene quantum dots (GQDs) and nitrogen-doped graphene quantum dots (NGQDs) were taken on mica sheets and are shown in Fig. S6(a3 and a4).† AFM surface profiles showed that the GQDs were in the size range of 5–10 nm. TEM micrographs of GQD and NGQDs are shown in Fig. S6(b3 and b4).† The BET surface area isotherms for AC, CNS, rGO are shown in Fig. 2(d–f) and corresponding BET surface area isotherms for CMS, GO, GQD, nGQD are shown in Fig. S6(c1–c4).† AC and rGO showed type IV hysteresis isotherm, CMS and GO showed the type III isotherms, while CNS had type II like isotherm.[23,24] The calculated surface areas for AC, CMS, CNS, GO, rGO were 933, 24, 51, 52, and 82 $m^2 g^{-1}$, respectively. Barrett–Joyner–Halenda (BJH) pore size distribution is shown in Fig. S5(b).†

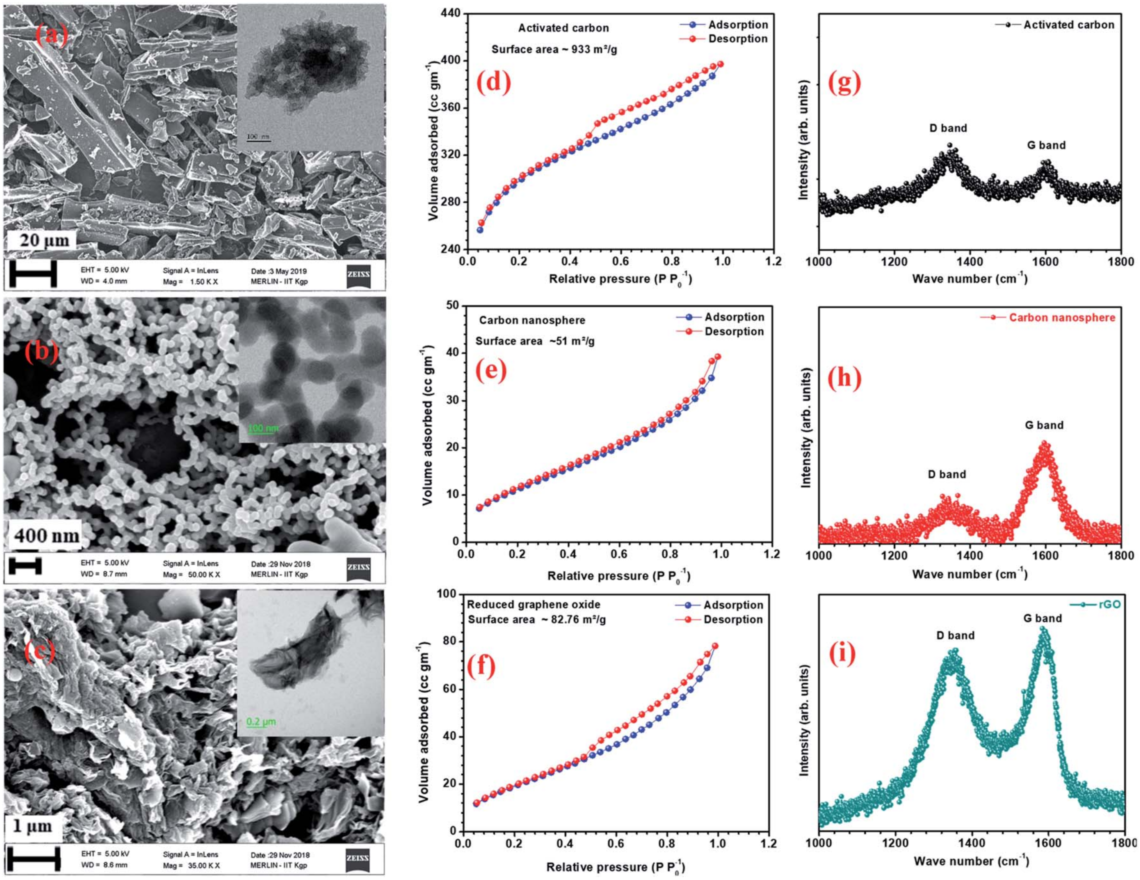

Fig. 2 (a–c) SEM micrographs, (insets of a–c) TEM micrographs; (d–f) BET N_2 adsorption desorption curve and (g–i) Raman spectra for activated carbon, carbon nanosphere, reduced graphene oxide, respectively.

Table 2 Degree of graphitization for carbon structures

Sample Name	AC	CMS	CNS	GO	rGO	GQDs	nGQDs
Degree of graphitization	1.02	0.086	0.45	0.96	0.87	0.77	1.97

The Raman spectra of AC, CNS and rGO are shown in Fig. 2(g–i) had two characteristic peaks *viz.*, one near 1595 cm^{-1} (G peak), which is the characteristic scattering peak of graphite and the second peak at 1350 cm^{-1} (D peak), that is caused by lattice defects, disordered arrangement, and the low symmetry.[25] The corresponding curves for CNS, GO, GQD and nGQD are shown in Fig. S6(d1–d4).† Particle size distribution for all the carbon structures are shown in Fig. S7.† The degree of graphitization can be calculated using the ratio of intensities of the D and G peaks. It is inversely proportional to the in-plane crystallite sizes (L_α) and is given by the Tuinstra–Koenig (TK) formula.[26]

$$R = \frac{I_G}{I_D}$$

and,

$$L_a = (2.4 \times 10^{-10})\lambda^4 \left[\frac{I_D}{I_G}\right]^{-1}$$

where R is the degree of graphitization of different carbon materials, I_G is the intensity of the G peak and I_D is the intensity of the D peak. A small value of the R indicates higher graphitization. λ is the Raman excitation wavelength. The G-band represents the C–C vibrational mode of the sp^2 hybridized carbon materials.[27] The G band forms due to the in-plane vibration of the carbon atom in E_{2g} symmetry.[28] The small peak at 1575 cm^{-1} can be linked to the oxidation of the graphite structure. The formation of broad D peaks near 2455 cm^{-1} for GO pointed towards the stacking of GO and rGO flakes. The blue shift was observed in the G band of the rGO, in comparison to the GO flakes.[29] The randomly stacked layers would promote the formation of a disordered array of multilayer GO and rGO. The formation of the multilayer GO and rGO were calculated by the intensity ratio of the G band and D band.[30] The ratio of the peak intensity of D- and G bands was 0.98, which is a measure of the defects present in the layer.[31] For GO and rGO, multilayer stacking was found to be 2 and 24, respectively.[16] Table 2 shows the degree of graphitization for each of the carbon structures. Further, Raman spectra of nitrogen-doped graphene quantum dot showed the characteristic peak of D band (1346 cm^{-1}) and G band (1596 cm^{-1}). The ratio of the peak intensity of D- and G bands was 1.34. In the case of NGQDs, the I_D/I_G ratio was slightly higher. This can be attributed to the hetero atom doping. The FTIR analysis is shown and discussed in ESI (Fig. S8(a)†).

Electrochemical results

The electrochemical performances of all the electrodes were investigated using 2 M NaOH aqueous electrolyte in 3-electrode configuration. Before the electrochemical measurements, to ensure complete soaking, the electrodes were pre-dipped in the electrolyte (2 M NaOH) solution for 20 min. $NaFePO_4$ was studied in the three-electrode in the potential window of −0.3 V to 0.5 V.[32] The CV and CD for $NaFePO_4$ are shown in Fig. 3(a and b). The specific capacitance of hollow $NaFePO_4$ structures was 125 F g^{-1}. In the charge–discharge study, these structures could deliver 142 F g^{-1} capacitance, at 1 A g^{-1} discharge current density. Variation of specific capacitance with scan rate and current density is shown in Fig. 3(d). The cycling stability test showed that the electrodes only lost 7% of the initial capacitance after 1500 cycles (Fig. 3(c)). This material showed higher performance than the other aqueous-based Na-ion electrode materials.[33,34] As the scan rate increased to 150 mV s^{-1}, the specific capacitance decreased to 40 F g^{-1}. Therefore, the capacitance retention was only 29%. When the discharging current increased by 5-folds, 55% specific capacitance was retained. This can happen because, when the scan rate or discharge current increases, the material has less time for storage or transfer, leading to reduced performance. The charge transport kinetics of the electrode was studied by the analysis of electrochemical impedance spectroscopy (EIS). Nyquist plots also give information about electrode–electrolyte interactions and equivalent series resistance (ESR). The ESR value for the hollow microsphere was 0.78 Ω (Fig. S9†).

In a hybrid device, there are two types of electrochemical charge storage mechanisms, which must be considered *viz.*, electric double layer capacitance (EDLC) and pseudocapacitance.[35] The total storage capacity for an electrode is

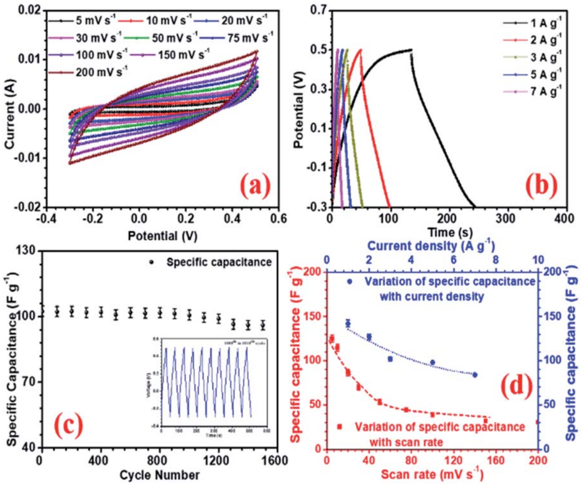

Fig. 3 (a) CV profiles at different scan rates, (b) CD profiles at different current density, (c) capacity fade with scan rate and current density and (d) cycling stability of $NaFePO_4$ in 2 M NaOH.

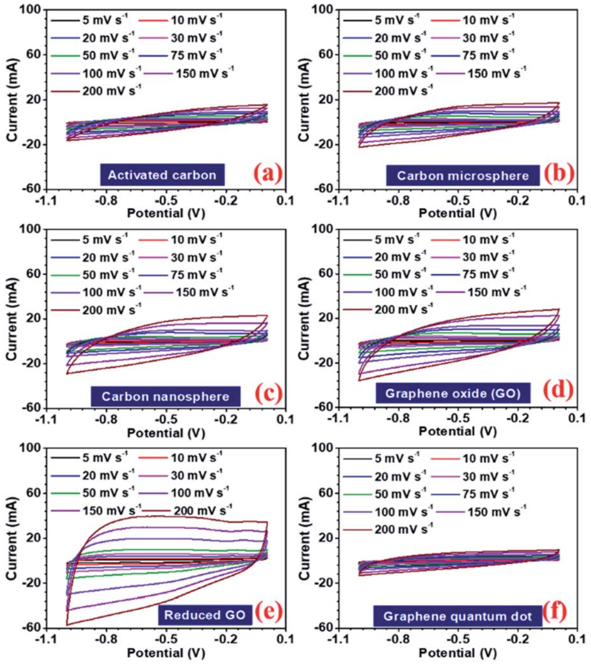

Fig. 4 CV profiles at different scan rates (a) activated carbon, (b) carbon microsphere, (c) carbon nanosphere, (d) graphene oxide (GO), (e) reduced graphene oxide (rGO), and (f) graphene quantum dot (GQD).

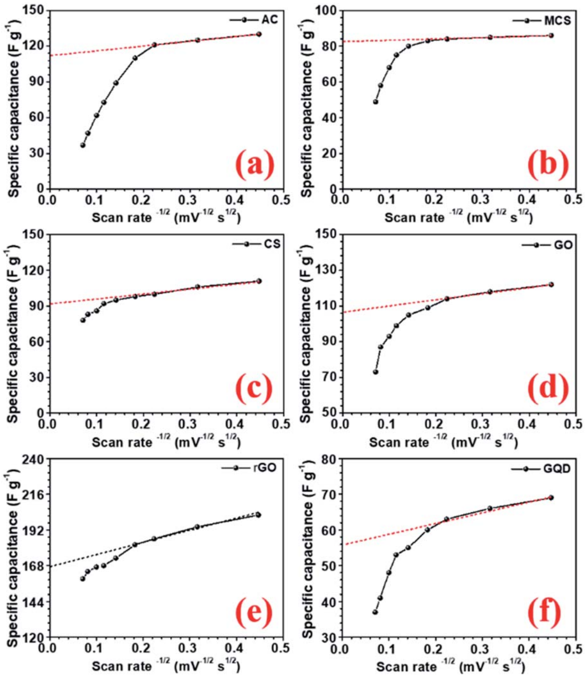

Fig. 5 CV profiles at different scan rates (a) activated carbon, (b) carbon microsphere, (c) carbon nanosphere, (d) graphene oxide (GO), (e) reduced graphene oxide (rGO), and (f) graphene quantum dot (GQD).

a convoluted picture of both these mechanisms, which are mainly controlled by (a) surface area, (b) porosity, (c) number of active sites, (d) presence of the functional group, and (e) availability of the redox-active sites in the electrode.[36,37] In this study, all the carbon structures showed a stable voltage window of -1 to 0 V, as shown in Fig. 4(a–f). Maximum specific capacitance values obtained from the CV curves at 5 mV s^{-1}, were 130, 86, 111, 122, 202, 69, and 77 F g^{-1} for AC, CMS, CNS, GO, rGO, GQD, and NGQD, respectively. The calculated specific capacitance, with increasing scan rates, is listed in Table 3.

The specific capacitance values decrease with the increase in scan rate, which is a normal behaviour in supercapacitor electrode materials. As the scan rate increases, the electrodes have less time to exploit the voltage window. Hence, the charge storage capacity decreases. Additionally, the electrochemical kinetics of the electrostatic adsorption in EDLC is slower than that of the pseudocapacitive faradaic reactions.[38] Consequently, the specific capacitance decreases as the material has less time to exchange charges *i.e.* faradaic reactions.[39] The quantification curves for the carbon structures are shown in Fig. 5. This allowed the estimation of the pseudocapacitance contribution in the electrode. Most of the curves showed a plateau region, which signifies materials having EDL type storage behaviour. Capacity retention was 36, 67, 74, 71, 81, 20, and 40% for AC, CMS, CNS, GO, rGO, GQD and NGQD, respectively (calculated from CV profiles). It can be seen from the quantification curves that reduced GO had highest pseudocapacitive contribution, in comparison to the other carbon structures.

Table 3 Values of specific capacitance with the increase of specific capacitance for different carbon structures from CV profiles

	Specific capacitance (F g^{-1})						
Scan rate (mV s^{-1})	AC	CMS	CNS	GO	rGO	GQD	NGQD
5	130	86	111	122	202	69	77
10	125	85	106	118	194	66	55
20	121	84	100	114	186	63	49
30	110	83	98	109	182	60	46
50	89	80	95	105	173	55	42
75	73	75	92	99	168	53	38
100	62	68	86	93	167	48	34
150	47	58	83	87	164	41	31

Table 4 Values of specific capacitance with the increase of specific capacitance for different carbon structures from CD profiles

	Specific capacitance (F g^{-1})						
Current density (A g^{-1})	AC	CMS	CNS	GO	rGO	GQD	nGQD
1	124	78	110	109	202	70	73
2	121	63	95	109	194	66	53
3	118	60	90	108	186	63	47
4	116	58	85	106	173	60	40
5	114	55	83	105	168	55	35
8	106	47	72	93	167	53	25
10	94	43	64	83	164	48	15

Table 5 Comparison of specific capacitance for different carbon-based electrodes and the capacity of varying device combinations

Material	3 electrode CV	3 electrode CD	2 electrode CV with NFP	2 electrode CD with NFP	ESR value of the device	R_{ct} values of the device
AC	130	124	23	23	2.43	15.53
Micro sphere	86	78	29	23	1.45	7.72
Nano sphere	111	110	39	32	1.06	7.02
GQD	69	70	24	25	1.43	6.17
NGQD	77	73	34	30	1.89	6.62
GO	122	109	44	40	2.1	5.54
rGO	202	180	58	63	3.56	5.42

The AC showed lower capacity retention compared to others. Modifying the carbon to micro and nanostructured spheres improved capacity retention, but the specific capacitance values remained lower than that of rGO. The highest specific capacitance value of AC material can be attributed to the largest surface area.[40] The higher capacitance retention for carbon nanostructure can be attributed to the higher zeta potential value.[41] The zeta potential values for different carbon structures are shown in Fig. S8(b).† GO flakes also showed EDLC type storage, but the higher surface area and zeta potential make this structure useful for supercapacitor applications. In the case of rGO, there are additional oxygen functional groups present amongst which carboxyl and phenol groups actively participate in the faradaic redox reactions, when placed in the alkaline electrolyte with hydroxyl ions (OH^-).[42] Therefore, rGO can show both EDLC, as well as pseudocapacitance. This induced higher specific capacitance values, in comparison to other carbonaceous materials. The corresponding charge transfer equations can be written as follows:[43]

$$-COOH + OH^- \leftrightarrow -COO^- + H_2O + e^-$$

$$\equiv C\text{–}OH + OH^- \leftrightarrow \rangle C\text{–}O^- + H_2O + e^-$$

The electrochemical performance of GQD and NGQD are shown in ESI.† The specific capacitance values determined from the charge–discharge profiles are listed in Table 4. The maximum specific capacitance was observed for rGO, which could deliver up to 220 F g^{-1} at 1 A g^{-1}. Maximum specific capacitance for the AC, CMS, CNS, GO, GQD and NGQD were 124, 78, 110, 109, 70, and 73 F g^{-1}, at 1 A g^{-1} current density. CD curves, variations in specific capacitance, as a function of increasing scan rate and current densities, are shown in Fig. S10–S12,† respectively. It was observed that, as the current density or scan rate increased, the specific capacitance decreased rapidly at first, and thereafter the rate slowed down. This behaviour also supports the hypothesis, which suggested the coexistence of EDLC and pseudocapacitance.

The performance of the carbon electrodes was also investigated by electrochemical impedance spectroscopy (EIS). Fig. S13† shows the EIS curve for the different carbon electrodes. rGO had the lowest electrochemical series resistance (ESR) value of 0.59 Ω. It also showed low charge transfer resistance, which again supports the increase in pseudocapacitance of the material.[44] The ESR values, Warburg resistance and the charge transfer resistance are listed in Table S1.† GQD and NGQD showed a dominant EDLC type behaviour.

Following the 3-electrode performance of the electrodes, asymmetric hybrid devices were also fabricated. Fabrication of asymmetric supercapacitor device needs charge balancing of the electrode materials. The optimal charge balance condition was estimated using the mass balance formula:[32]

$$\frac{m_+}{m_-} = \frac{\Delta V_- C_-}{\Delta V_+ C_+}$$

where C_- and C_+ are the capacitances (in F g^{-1}) measured at the same scan rate, using the three-electrode system, while ΔV_+ and ΔV_- denote the potential working window for the positive and negative electrodes, respectively. The required mass ratio for positive and negative electrodes (m_+/m_-) was estimated at 5 mV s^{-1} and the total mass ($m_+ + m_-$) was set to 2.0 mg cm^{-2} for each device. To utilize the full electrochemical window in the device, positive electrode material ($NaFePO_4$) was combined with each negative electrode material (*i.e.* carbon variants). The operation window was also optimized for the hybrid devices.

$NaFePO_4$//AC showed stable performance in the 1.3 V voltage window. CV curves for all the devices fabricated using carbon structures (except NFP//rGO) are shown in Fig S15.† As the structures changed to CMS and CNS, the voltage window increased to 1.7 V. NFP//AC device could deliver 23 F g^{-1} specific capacitance at a 5 mV s^{-1} scan rate. So, shifting from microstructures of AC to spherical structures helped to achieve asymmetric supercapacitors with a higher voltage window. The highest specific capacitance observed in the NFP//CMS and NFP//CNS devices were 29 F g^{-1} and 39 F g^{-1}, respectively, at 5 mV s^{-1}.

Charge discharge results also corroborated the CV studies. CD curves, at increasing current densities, in devices with different carbon structures (except NFP//rGO), are shown in Fig S16.† NFP//AC could deliver up to 23 F g^{-1} specific capacitance at 1 A g^{-1} discharging current density. In comparison, NFP//CNS could deliver up to 32 F g^{-1} at 1 A g^{-1} current density. NFP//GO based asymmetric device delivered a maximum specific capacitance of 44 F g^{-1} and 40 F g^{-1} at 5 mV s^{-1} scan rate and 1 A g^{-1} current density, respectively. Higher specific

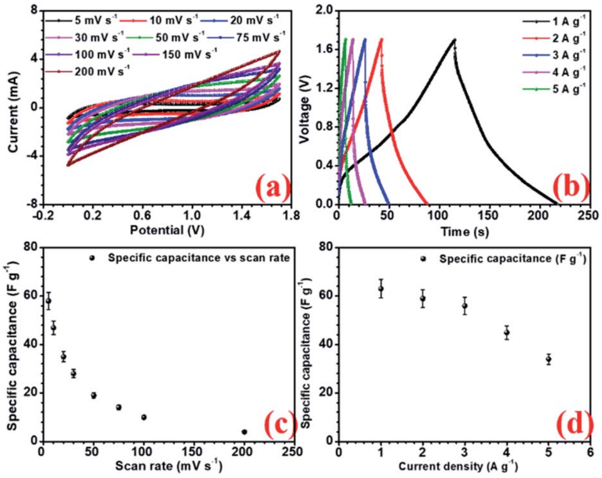

Fig. 6 (a) CV profiles at different scan rate, (b) charge discharge at different current density, (c) decrease specific capacitance with increase in scan rate and, (d) variation of specific capacitance with current density for $NaFePO_4$//rGO device.

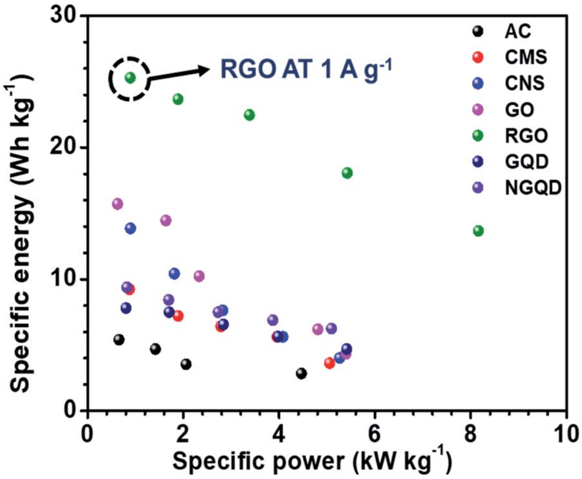

Fig. 7 The Ragone plot for the different combinations of devices.

capacitance can be attributed to the layered structures of the GO, where it can accommodate more Na-ions in the bulk of the material and provides a greater number of channels for the ions to interact with material and store charge. The electrochemical results for n-GQD are shown in Fig. S14.†

Amongst all the asymmetric device configurations, the NFP//rGO combination gave the best results. Corresponding CV and CD curves at increasing scan rate and current density are shown in Fig. (6a and b). Here the device could deliver up to 58 F g^{-1} and 63 F g^{-1} specific capacitance at 5 mV s^{-1} scan rate and 1 A g^{-1} current density, respectively, without compromising the voltage window, which has been found to be 1.7 V. rGO provided improved EDLC nature owing to higher surface area and positive higher zeta potential value, which enhances the charge storage.

Again, the layered structures of the rGO can accommodate a higher amount of Na^+ ions on the surface as well as in the interior of the layered structures. So, compared to the other carbon structures with simpler morphologies, layered rGO can suitably combine with the NFP electrode and provide the required performance to achieve a well-performing device with high charge storage. This device can compete well with some of the suggested Na-ion or metal oxide-based supercapacitors, as shown in Table 5. GQD and NGQD showed reduced performance as they could show only 25 and 30 F g^{-1} specific capacitance in device configuration with $NaFePO_4$. The electrochemical impedance spectroscopy (EIS) was investigated within a frequency range of 50 mHz to 1 MHz. The corresponding results are shown in SI (Fig. S14†). Among the carbon structures, the NFP//rGO device showed low ESR (R_s) and the lowest charge transfer resistance (R_{ct}) at the electrode–electrolyte interface (EEI). Low R_{ct} signifies that NFP//rGO had low resistance, and rGO facilitates solvated Na^+ ions to intercalation into the interlayer spacing while ensuring efficient charge transfer from the electrolyte to the bulk of the material. NFP//rGO based asymmetric device also had the lowest ESR values (Table 5).

Table 6 Comparison of specific capacitance for different carbon-based electrodes and the capacity of varying device combinations

Work	Energy density (W h kg^{-1})	Reference
$NaMnO_2$//AC	19.5	33
$NaMnO_2$//AC	28.56	45
$Na_{0.21}MnO_2$//AC	31.8	46
$NaMnPO_4$//AC	10.7	47
CuO//AC	19.7	48
RuO_2//rGO	26.3	49
MnO_2//Graphene	6.8	50
$Na_2Ti_2O_{5-x}$//rGO-AC film	15.6	51
$NaMn_{1/3}Ni_{1/3}Co_{1/3}PO_4$//AC	15	52
$NaMn_{1/3}Ni_{1/3}Co_{1/3}PO_4$//AC	50	53
$NaFePO_4$//rGO	25.29	This work

The ESR and charge transfer resistance values for all the combinations are shown in Table 5. The Ragone plot for the different combinations is shown in Fig. S17.† The highest energy density was achieved by the $NaFePO_4$//rGO device and the value was 25.29 W h kg^{-1} and power density was 0.894 kW kg^{-1} (Table 6). The comparison of power density and energy

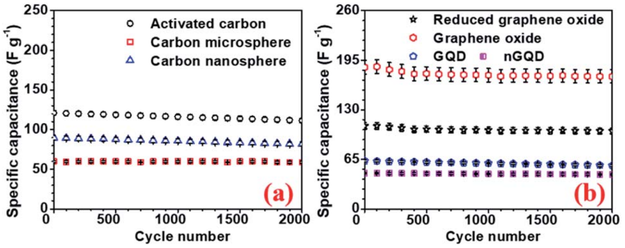

Fig. 8 Cycling stability test for (a) AC, CMS, CNS and (b) GO, rGO, GQD, nGQ electrodes, respectively.

density for all the device configurations are listed in Table S4† (Fig. 7).

To investigate the performance of the supercapacitor cycling stability of the electrode and the devices were also tested. All carbon-based electrodes were subjected to a cycling stability test for 2000 cycles and the corresponding results, for different electrodes are, presented in Fig. 8. rGO electrodes showed 94% capacity retention after 2000 cycle with the highest specific capacitance. The device with hollow $NaFePO_4$//rGO showed 87% capacity after 2000 cycles.

Conclusions

Hollow $NaFePO_4$ structures, with various carbon structures, can be utilized to fabricate Na-ion supercapacitors. Carbon structures (1-, 2-, 3-D types) are tested as negative electrodes in the device. Different combinations lead to varied performance, which indicates that the choice of complementary carbon electrodes is critical in Na-ion-based storage technologies. Reduced GO showed the best performance in devices with NFP structures. $NaFePO_4$//rGO combination can deliver specific capacitance 63 F g^{-1} at 1 A g^{-1} current density, which is nearly three times higher than the NFP//AC based device. The device also retained 87% cycling stability after 2000 cycles of charge–discharge. An optimized device can deliver energy and power density values, which can make Na-ion supercapacitors a competitive technology with good cycling stability.

Conflicts of interest

There are no conflicts to declare.

Acknowledgements

The authors acknowledge the central research facility, Indian Institute of Technology Kharagpur for the all support for acquiring experimental data. (AC) would like to acknowledge DST (India) for supporting the establishment of experimental facilities under its Materials for Energy Storage (MES) scheme for the project entitled, "Hierarchically nanostructured energy materials for next generation Na-ion based energy storage technologies and their use in renewable energy systems".

Notes and references

1 J. Nai and X. W. D. Lou, *Adv. Mater.*, 2019, **31**, e1706825.
2 M. Minakshi and D. Meyrick, *J. Alloys Compd.*, 2013, **555**, 10–15.
3 V. Aravindan, M. Ulaganathan and S. Madhavi, *J. Mater. Chem. A*, 2016, **4**, 7538–7548.
4 Y. Yuan, C. Wang, K. Lei, H. Li, F. Li and J. Chen, *ACS Cent. Sci.*, 2018, **4**, 1261–1265.
5 S. Biswas, V. Sharma, T. Singh and A. Chandra, *J. Mater. Chem. A*, 2021, **9**, 6460–6468.
6 D. Mandal, S. Biswas, A. Chowdhury, D. De, C. S. Tiwary, A. N. Gupta, T. Singh and A. Chandra, *Nanotechnology*, 2021, **32**, 025504.
7 X. Li, Y. Chen, H. Huang, Y.-W. Mai and L. Zhou, *Energy storage materials*, 2016, **5**, 58–92.
8 M. Galceran, V. Roddatis, F. J. Zúñiga, J. M. Pérez-Mato, B. Acebedo, R. Arenal, I. Peral, T. Rojo and M. Casas-Cabanas, *Chem. Mater.*, 2014, **26**, 3289–3294.
9 M. R. Bonilla, A. Lozano, B. Escribano, J. Carrasco and E. Akhmatskaya, *J. Phys. Chem. C*, 2018, **122**, 8065–8075.
10 W. Tang, X. Song, Y. Du, C. Peng, M. Lin, S. Xi, B. Tian, J. Zheng, Y. Wu, F. Pan and K. P. Loh, *J. Mater. Chem. A*, 2016, **4**, 4882–4892.
11 K. T. Lee, T. N. Ramesh, F. Nan, G. Botton and L. F. Nazar, *Chem. Mater.*, 2011, **23**, 3593–3600.
12 S. Kandhasamy, K. Nallathamby and M. Minakshi, *Prog. Solid. State Ch.*, 2012, **40**, 1–5.
13 C. Kanade, S. Arbuj, K. Kanade, K. S. Kim, G. Y. Yeom, T. Kim and B. Kale, *RSC Adv.*, 2018, **8**, 39749–39755.
14 A. Chandra, A. J. Roberts and R. C. T. Slade, *Solid State Commun.*, 2008, **147**, 83–87.
15 S. Biswas, V. Sharma, D. Mandal, A. Chowdhury, M. Chakravarty, S. Priya, C. C. Gowda, P. De, I. Singh and A. Chandra, *CrystEngComm*, 2020, **22**, 1633–1644.
16 S. Ghosh, D. Mandal, A. Chandra and S. N. B. Bhaktha, *J. Light. Technol.*, 2019, **37**, 2380–2385.
17 D. De, C. K. Das, D. Mandal, M. Mandal, N. Pawar, A. Chandra and A. N. Gupta, *ACS Appl. Bio Mater.*, 2020, **3**, 6284–6296.
18 A. Chowdhury, A. Dhar, S. Biswas, V. Sharma, P. S. Burada and A. Chandra, *J. Phys. Chem. C*, 2020, **124**, 26613–26624.
19 R. Heimbockel, F. Hoffmann and M. Froba, *Phys. Chem. Chem. Phys.*, 2019, **21**, 3122–3133.
20 C. Murugesan, S. Lochab, B. Senthilkumar and P. Barpanda, *ChemCatChem*, 2018, **10**, 1122–1127.
21 X. Jiao, Y. Qiu, L. Zhang and X. Zhang, *RSC Adv.*, 2017, **7**, 52337–52344.
22 D. Bergna, T. Varila, H. Romar and U. Lassi, *C*, 2018, **4**, 41.
23 H. Li, L. Sun, Y. Zhang, T. Tan, G. Wang and Z. Bakenov, *J. Energy Chem.*, 2017, **26**, 1276–1281.
24 R. Liu, T. Gong, K. Zhang and C. Lee, *Sci. Rep.*, 2017, **7**, 9761.
25 J. B. Wu, M. L. Lin, X. Cong, H. N. Liu and P. H. Tan, *Chem. Soc. Rev.*, 2018, **47**, 1822–1873.
26 P. Mallet-Ladeira, P. Puech, C. Toulouse, M. Cazayous, N. Ratel-Ramond, P. Weisbecker, G. L. Vignoles and M. Monthioux, *Carbon*, 2014, **80**, 629–639.
27 F. Negri, E. di Donato, M. Tommasini, C. Castiglioni, G. Zerbi and K. Mullen, *J. Chem. Phys.*, 2004, **120**, 11889–11900.
28 J. H. Kaufman, S. Metin and D. D. Saperstein, *Phys. Rev. B. Condens. Matter.*, 1989, **39**, 13053–13060.
29 K. Tsirka, A. Katsiki, N. Chalmpes, D. Gournis and A. S. Paipetis, *Front. Mater.*, 2018, **5**, 37.
30 S. Pei and H.-M. Cheng, *Carbon*, 2012, **50**, 3210–3228.
31 A. Dey, S. Krishnamurthy, J. Bowen, D. Nordlund, M. Meyyappan and R. P. Gandhiraman, *ACS Nano*, 2018, **12**, 5473–5481.
32 S. Biswas, A. Chowdhury and A. Chandra, *Front. Mater.*, 2019, **6**, 54.

33 Q. T. Qu, Y. Shi, S. Tian, Y. H. Chen, Y. P. Wu and R. Holze, *J. Power Sources*, 2009, **194**, 1222–1225.

34 B. Senthilkumar, K. V. Sankar, L. Vasylechko, Y.-S. Lee and R. K. Selvan, *RSC Adv.*, 2014, **4**, 53192–53200.

35 Poonam, K. Sharma, A. Arora and S. K. Tripathi, *J. Energy Storage*, 2019, **21**, 801–825.

36 C. Zheng, X. F. Zhou, H. L. Cao, G. H. Wang and Z. P. Liu, *J. Mater. Chem. A*, 2014, **2**, 7484.

37 M. A. Akhtar, A. Chowdhury and A. Chandra, *J. Phys. D Appl. Phys.*, 2019, **52**, 155501.

38 J.-S. M. Lee, M. E. Briggs, C.-C. Hu and A. I. Cooper, *Nano Energy*, 2018, **46**, 277–289.

39 S. N. Khatavkar and S. D. Sartale, *New J. Chem.*, 2020, **44**, 6778–6790.

40 O. Barbieri, M. Hahn, A. Herzog and R. Kötz, *Carbon*, 2005, **43**, 1303–1310.

41 Z. Lei, Z. Liu, H. Wang, X. Sun, L. Lu and X. S. Zhao, *J. Mater. Chem. A*, 2013, **1**, 2313.

42 N. H. Khdary, M. E. Abdesalam and G. El Enany, *J. Electrochem. Soc.*, 2014, **161**, G63–G68.

43 Q. Li, M. Horn, Y. Wang, J. MacLeod, N. Motta and J. Liu, *Materials*, 2019, **12**.

44 M. R. Hasyim and R. Rajagopalan, *J. Electrochem. Soc.*, 2020, **167**, 013536.

45 S. Xu, T. Wan, K.-b. Zhou, G.-m. Zhu, Z.-q. He, H.-b. Huang, T. Zhou, W.-q. Mao, J.-j. Wu, S.-k. Gong and Y.-x. Qiao, *Mater. Res. Express*, 2020, **7**, 035508.

46 N. Karikalan, C. Karuppiah, S. M. Chen, M. Velmurugan and P. Gnanaprakasam, *Chemistry*, 2017, **23**, 2379–2386.

47 A. Chowdhury, S. Biswas, T. Singh and A. Chandra, *Electrochem. Sci. Adv.*, 2021, e2100030.

48 S. E. Moosavifard, M. F. El-Kady, M. S. Rahmanifar, R. B. Kaner and M. F. Mousavi, *ACS Appl. Mater. Interfaces*, 2015, **7**, 4851–4860.

49 J. T. Zhang, J. W. Jiang, H. L. Li and X. S. Zhao, *Energy Environ. Sci.*, 2011, **4**, 4009–4015.

50 Y. He, W. Chen, X. Li, Z. Zhang, J. Fu, C. Zhao and E. Xie, *ACS Nano*, 2013, **7**, 174–182.

51 L.-F. Que, F.-D. Yu, K.-W. He, Z.-B. Wang and D.-M. Gu, *Chem. Mater.*, 2017, **29**, 9133–9141.

52 M. Minakshi, D. Meyrick and D. Appadoo, *Energy Fuels*, 2013, **27**, 3516–3522.

53 M. M. Sundaram, T. Watcharatharapong, S. Chakraborty, R. Ahuja, S. Duraisamy, P. T. Rao and N. Munichandraiah, *Dalton Trans.*, 2015, **44**, 20108–20120.